Preliminary site characterization for earthquake hazard assessment using ambient vibration techniques in Haines Junction, Yukon (parts of NTS 115A/11, 12, 13, 14)

*Tess Leishman**
School of Earth and Ocean Sciences, University of Victoria

Jeremy M. Gosselin and Jan Dettmer
Department of Earth, Energy, and Environment, University of Calgary

John F. Cassidy
Geological Survey of Canada, Natural Resources Canada
School of Earth and Ocean Sciences, University of Victoria

Tae-Seob Kang
Division of Earth Environmental System Science, Pukyong National University, South Korea

Leishman, T., Gosselin, J.M., Dettmer, J., Cassidy, J.F. and Kang, T.-S., 2024. Preliminary site characterization for earthquake hazard assessment using ambient vibration techniques in Haines Junction, Yukon (parts of NTS 115A/11, 12, 13, 14). *In*: Yukon Exploration and Geology Technical Papers 2023, L.H. Weston and Purple Rock Inc. (eds.), Yukon Geological Survey, p. 57–76.

Abstract

Regional mapping of soil stiffness improves understanding of seismic hazard in northern Canada, specifically southwestern Yukon, where local amplification hazards are largely unknown. Ambient vibration (AV) measurements record microtremor seismic noise used to calculate the horizontal-to-vertical spectral ratio (HVSR) and identify resonant frequencies at sites. *In-situ* estimation of fundamental frequency (f_0) is used to characterize sites and map local site amplification hazards. Furthermore, AV measurements permit the estimation of surface-wave propagation speeds at different frequencies (*i.e.*, dispersion). Dispersion measurements are used to infer profiles of shear-wave velocity as a function of depth. We present preliminary site characterization using AV measurements from 23 measured sites in Haines Junction, Yukon. The preliminary results suggest a spatial trend of fundamental frequency laterally, where higher frequencies are identified north of Haines Junction and lower f_0 values are identified in south-central Haines Junction. We attribute these observations to the proximity to the Dezadeash River basin.

Introduction

Haines Junction is located in southwestern Yukon, a region of complex active tectonics and abundant seismicity (Nelson *et al.*, 2013). Tectonics are governed by the oblique collision and subduction of the Yakutat microplate beneath the North American Plate (Bruhn *et al.*, 2012), which forms the high topography of the St. Elias Mountains in the region. The village of Haines Junction is at the base of this mountain range (Fig. 1). The St. Elias Mountains are heavily glaciated and characterized by large, crustal-scale faults with significant seismic activity (Doser and Rodriguez, 2011; Meighan *et al.*, 2013; Biegel *et al.*, 2023). The region

* tessleishman@uvic.ca
‡ jan.dettmer@ucalgary.ca

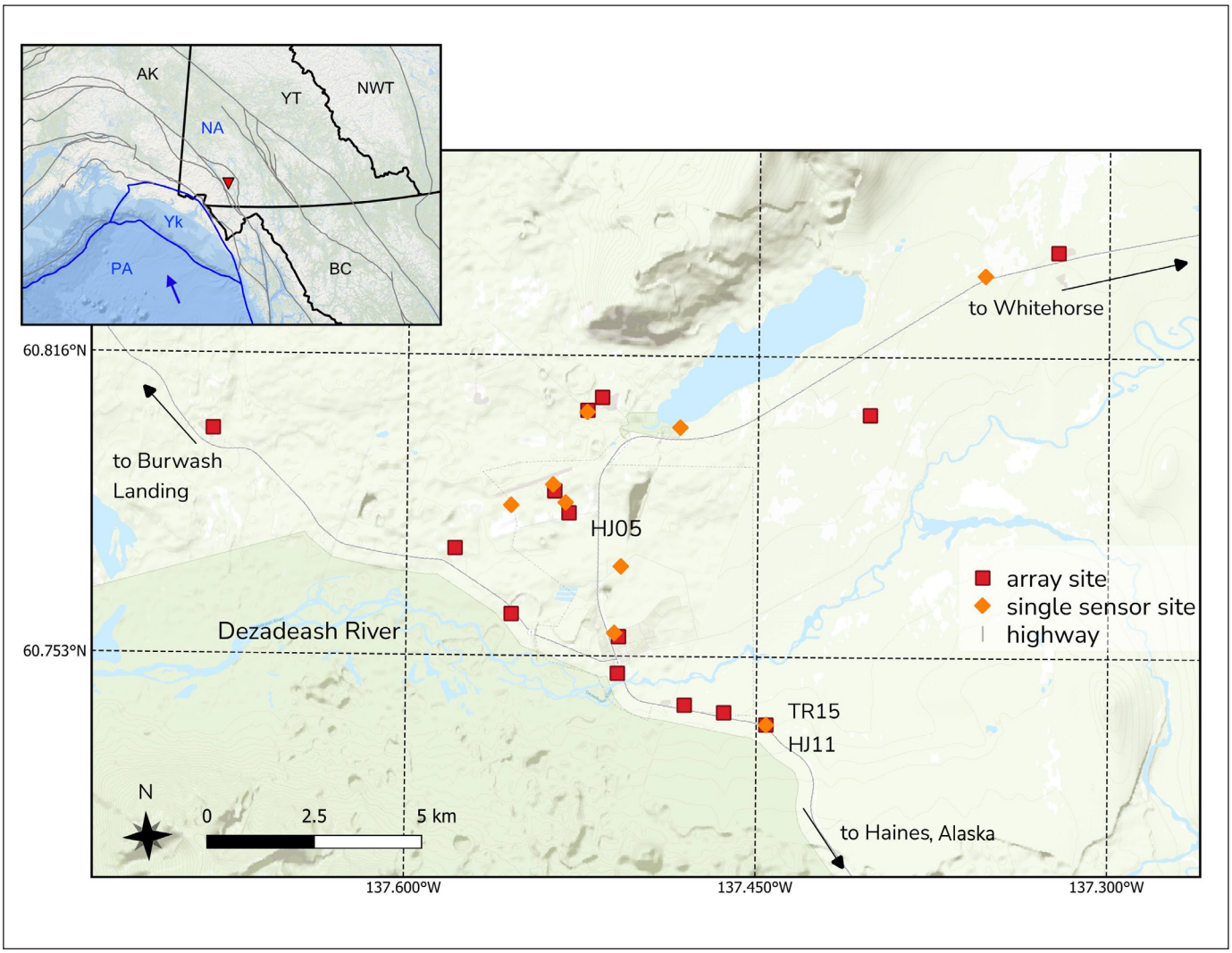

Figure 1. *Site locations for 23 passive seismic recordings in the Haines Junction area. Labelled sites HJ05, HJ11 and TR15 are discussed in the paper. Inset map shows the location of Haines Junction in southwestern Yukon (red triangle), a region of complex active tectonic interactions between the Pacific (PA), Yakutat (Yk) and North American (NA) plates. Tectonic boundaries and major regional faults are shown in blue and grey, respectively (after Yukon Geological Survey, 2020). Small blue arrow illustrates the plate vector of PA relative to NA (Kreemer et al., 2014). Political boundaries are shown in black.*

also exhibits high rates of uplift, erosion and exhumation (Enkelmann et al., 2009; Turner et al., 2016). As a result of these dynamic geological processes, the village of Haines Junction and the surrounding areas are susceptible to associated natural hazards. These include site-specific seismic amplification and resonance hazards, as well as liquefaction and landslide-related hazards. This paper presents preliminary investigations toward characterizing seismic site conditions using ambient vibration (AV) methods based on background seismic noise recordings from processes such as wind, waves and human activity.

Seismic hazard varies greatly across Canada, and the extent of our seismic hazard knowledge varies with geographic location and population density. Seismic hazard is modelled probabilistically by Natural Resources Canada based on seismic sources, fault types and site conditions (Adams et al., 2019; Kolaj et al., 2020). These models assume a given site classification and require adjustment based on local site conditions (V_{S30}, which is the time-averaged shear wave velocities in the upper 30 m of the crust); therefore, more detailed knowledge of local site effects is needed to accurately estimate the local seismic hazard. In densely populated regions, the local subsurface geology is relatively well

understood and seismic hazard is robustly modelled (Kolaj et *al*., 2020). Regions of low population density are generally poorly understood; site characterization and seismic hazard estimation in these areas largely rely on sparse historical earthquake records and surface topography as proxies. This is especially true for Canada's northern territories and Arctic region, where the presence of a hard permafrost layer has led to the assumption that northern Canada is generally not at risk of amplified shaking (Lamontagne and Bent, 2021). Efforts have been made to identify fault sources to accurately model seismicity in and around the Yukon (Allen et *al*., 2015); however, subsurface conditions remain broadly unknown, particularly in the more densely populated regions of Whitehorse and Haines Junction. Specifically, there has been no attempt to identify site effects in the Haines Junction area, despite local geological features that suggest the community is potentially at risk of laterally varying amplified and resonating earthquake shaking (Rampton and Paradis, 1979; Hunter and Crow, 2015).

The Yukon Geological Survey (YGS) has characterized surficial and bedrock geology in the Haines Junction region through multiple projects over decades to increase the granularity of mapping beyond regional work. The geology in southwestern Yukon is characterized by tectonic stacking of large rock assemblages dipping northeast (Israel et *al*., 2017). Metamorphic and igneous rocks outcrop directly northeast of Haines Junction, whereas southwest, toward the Denali fault, there are sedimentary and volcanic outcrops. Repeated Pleistocene glaciation covered the Haines Junction area with complex assemblages of till, glaciolacustrine and glaciofluvial sediments (Rampton and Paradis, 1979). During the Holocene, permafrost aggraded sporadically in the region, and organic veneers formed in the wetter valley bottoms and on the cooler aspect slopes. Little Ice Age advances in the St. Elias Mountains repeatedly impounded the Alsek River and deposited silty glaciolacustrine sediments throughout the Haines Junction townsite as recently as 1848 CE (Clague and Rampton, 1982).

The distribution of permafrost is not well understood, and soil stiffness and site amplification are likely variable throughout the region. Water well records (Government of Yukon, 2002) indicate the presence of a small subsurface basin filled with soft sediment deposited by the Dezadeash River, which runs through central Haines Junction. In addition to surficial mapping, YGS attempted to identify subsurface permafrost in Haines Junction using electrical resistivity methods (P. Lipovsky, pers. comm., 2021). Resistivity data collected using these methods have identified several sites where permafrost is inferred to exist. The YGS has a network of boreholes for monitoring permafrost conditions in Haines Junction, ranging in depth from 2 to 27 m.

There is currently a lack of seismic hazard identification in the Yukon, including limited knowledge of local hazard variation based on soil conditions (Kolaj et *al*., 2020; Lamontagne and Bent, 2021). Considering the notable seismicity in southwestern Yukon and potential for increased seismic hazard related to local site amplification (Rampton and Paradis, 1979; Hunter and Crow, 2015), communities in these regions face significant but unquantified levels of earthquake-related hazards. The horizontal-to-vertical spectral ratio (HVSR) technique (Nakamura, 1989) estimates the ratio between the horizontal and vertical components of ambient seismic noise. This technique is an established method for estimating the fundamental frequency (f_0) of a site to constrain the depth to significant seismic impedance contrasts (*i.e.*, soil layering structure) and, to a lesser extent, soil stiffness properties (Hunter and Crow, 2015). In this paper, we calculate HVSRs using recorded time series of microtremor waveforms to characterize sites in the Haines Junction region. We provide preliminary hazard assessments for 23 measured sites in the Haines Junction area (Fig. 1) as part of a larger study by YGS to accomplish a robust analysis of seismic hazard in the region using seismic response modelling. Low-frequency f_0 values (0.3–0.8 Hz) were identified at many sites, suggesting thick (*i.e.*, hundreds of metres) sequences of relatively soft sediment in certain areas, and associated risk of amplified shaking during an earthquake (Hunter and Crow, 2015). High-frequency HVSR peaks (10–50 Hz) were also identified at many sites, suggesting shallow, complex, soil-layering structures at depths of approximately 3–15 m. Furthermore, we measured surface-wave dispersion at 14 multi-instrument (array) sites throughout the region. Surface-wave dispersion data were used to probabilistically infer soil properties, and we present preliminary results from this analysis. Mapping these measurements improves our understanding of seismic hazard levels and distribution in southwestern Yukon.

Methods

Data collection

Data for this study were recorded at 23 sites in the Haines Junction region between July 2 and 6, 2023. Ambient vibration arrays (17 synchronous instruments) were deployed at 14 sites (Fig. 1), in cross-shape configurations with a 120 m diameter. The instruments used were Güralp 40T and Nanometrics Trillium Compact three-component (vertical, east and north) broadband seismometers. Figure 2a and b show array deployments at two sites, and Figure 2c shows a typical instrument installation. Ambient vibration recordings were taken at the remaining nine sites (Fig. 1) using a single three-component Tromino seismometer (Fig. 2d).

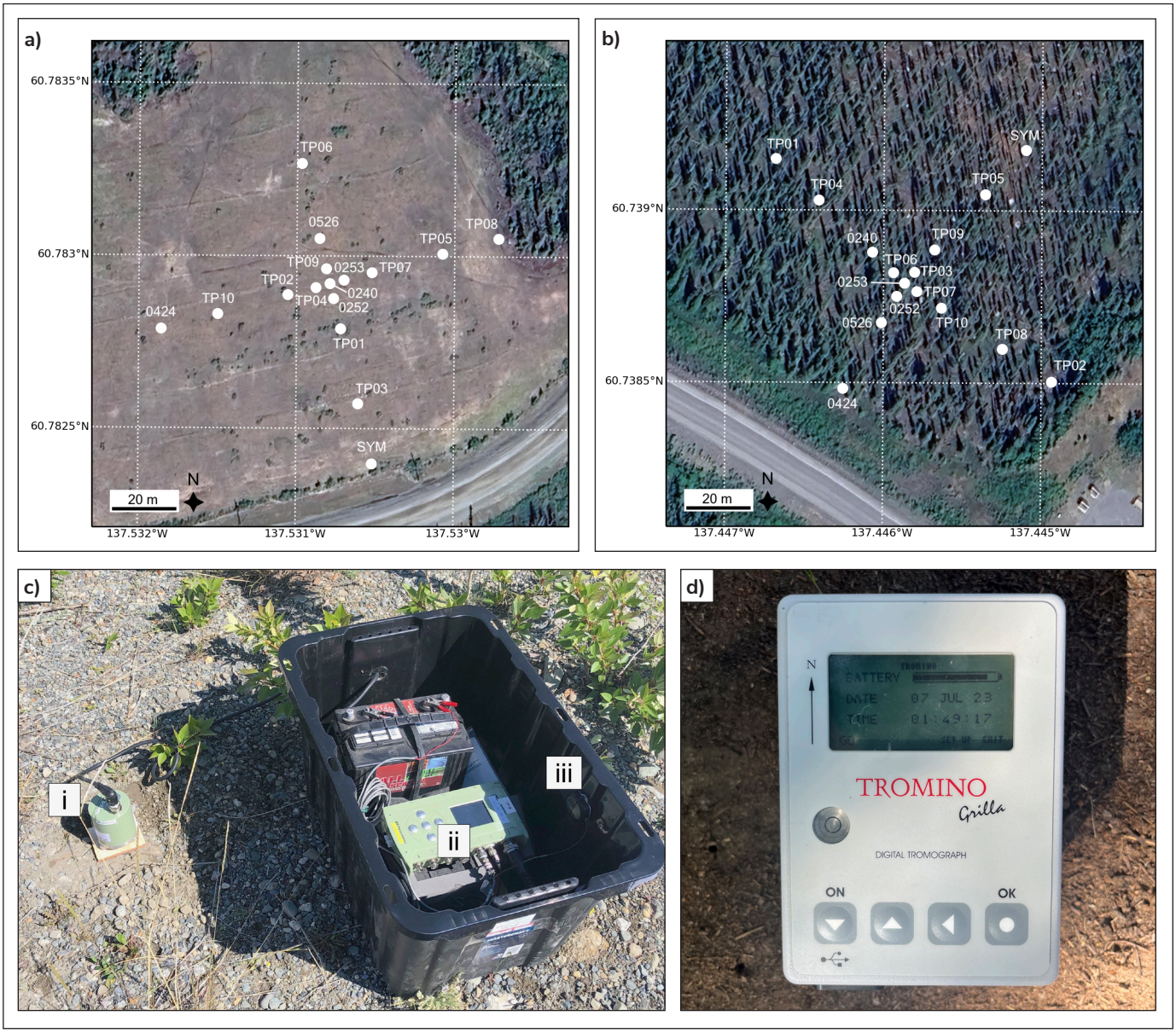

Figure 2. *Passive seismic array deployment configurations at sites* ***a)*** *HJ05 and* ***b)*** *HJ11. Individual instrument locations are shown in white. Recordings from instruments TP08 and SYM at both sites were not included in this work for technical reasons. Instruments are positioned along four arms/branches and are spaced at approximately 5, 15, 40 and 60 m from the centre of the array.* ***c)*** *Broadband seismograph deployment. Temporary, non-invasive installation includes a three-component sensor (seismometer) that is mechanically coupled to surficial soil using a ceramic plate (i); a digital recorder where data are saved (ii); and a GPS antenna to achieve exact, synchronous timing for data recording (iii).* ***d)*** *A three-component Tromino seismometer.*

Array AV recordings were approximately 2–3 h long with a sampling frequency of 100 Hz. These recordings captured broadband frequencies required for modelling purposes beyond the scope of this paper. Single-station Tromino recordings were 30 min long with a sampling frequency of 128 Hz to capture broadband frequencies excited by shallow and deep soil layering in the subsurface. These measurement criteria were chosen in accordance with SESAME (Site EffectS assessment using AMbient Excitations) guidelines for HVSR analysis (SESAME, 2004). Sites were selected based on various factors, including the presence of preliminary community-scale surficial geology mapping and results of electrical resistivity surveys provided by YGS (P. Lipovsky, pers. comm., 2021). Site selection was further guided by accessibility, availability and proximity to inhabited areas.

Horizontal-to-vertical spectral ratio processing

To obtain HVSR curves from AV recordings, time series from all three components (east, north and vertical channels) were extracted from each individual instrument. The ratios of horizontal and vertical recordings from each instrument were computed using Geopsy software (Wathelet *et al.*, 2020). Prior to calculating HVSR, recordings were corrected to account for the unique response of each instrument type. The signals, originally recorded in the time domain, were converted to the frequency domain as Fourier amplitude spectra for the three directional components using the discrete Fourier transform calculation (equation 1),

$$Y_k = \sum_{j=0}^{n-1} X_j \exp\left(-2\pi \frac{\sqrt{-1}}{n} jk\right) \qquad (1)$$

where array Y, containing the frequency values indexed by $0 \leq k < n$, is computed for array X (a time series of length n) with complex exponents for the various frequencies (Frigo and Johnson, 2005). For a robust analysis, recordings were divided into many time windows (Fig. 3a) so that the frequency spectra of each time window (Fig. 3b–d) produced an individual HVSR measurement (Fig. 3e). Based on SESAME criteria (SESAME, 2004), the length and number of windows is directly related to the resolution quality of the lowest frequency of interest. With the assumption that frequencies of interest are above 0.1 Hz, signals recorded from all channels were divided into 120 s window lengths (Fig. 3a). A relative sampling threshold of 75% was applied to exclude transient signals with abnormally high amplitudes. A 0.1 Hz high-pass filter was also applied to minimize the effect of tapering caused by windowing, which can distort the HVSR calculation in the presence of high-amplitude, low-frequency signals (SESAME, 2004). The HVSR (Fig. 3e) was then calculated by dividing the horizontal components of the 'windowed' frequencies by the vertical components to extract only the site response, eliminating the frequency response of the signal and the source (Nakamura, 1989). An average HVSR was computed from all the sensors at a site to produce a single representative HVSR curve. The HVSR curve of each sensor was analyzed individually to identify changes in resonant frequencies spatially over the site area. Sensors that produced outlier HVSR curves were removed from the calculation of the representative HVSR curve.

Surface-wave dispersion processing

Surface waves are seismic waves that propagate along Earth's free surface where it contacts the atmosphere. The propagation speed of these waves depends on the geophysical properties of the shallow subsurface (predominantly shear-wave velocity; V_S); however, the depth to which these waves are sensitive to site properties is a function of wavelength (or frequency). Low-frequency waves are sensitive to V_S at greater depths; consequently, surface waves with different frequencies will propagate (*i.e.*, disperse) at different velocities due to local vertically heterogeneous properties. The velocity–frequency relationship (*i.e.*, dispersion curve) can be used to infer profiles of geophysical site conditions, which is valuable for seismic site characterization. Surface-wave dispersion is generally more informative than HVSR curves for constraining site V_S conditions; however, the two provide complementary information (*e.g.*, Gosselin *et al.*, 2022). Surface-wave dispersion is sensitive to depth-integrated V_S, whereas HVSR curves are sensitive to seismic impedance contrasts (*i.e.*, discrete layer boundaries).

Several techniques exist for estimating surface-wave dispersion at a site. Rayleigh waves (a surface wave polarized in the vertical plane) generally dominate background/ambient seismic noise (Shapiro and Campillo, 2004); therefore, an attractive approach to estimate dispersion is to extract fundamental-mode

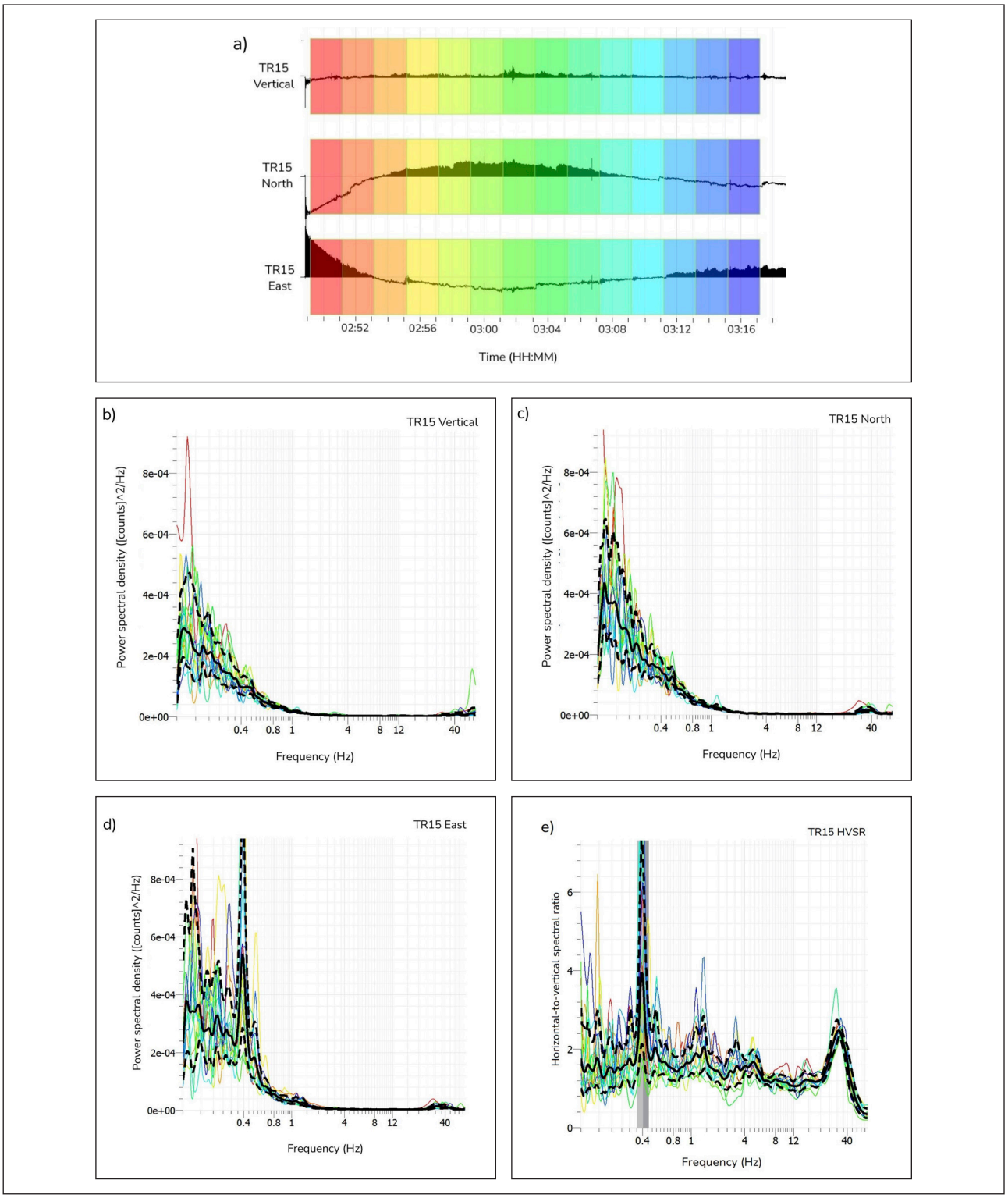

Figure 3. *Data analysis of site TR15.* ***a)*** *Time series windowing of site TR15 for spectra and horizontal-to-vertical spectral ratio (HVSR) calculations using 120 s windowing intervals of a 30 min Tromino recording. The colour of the recording windows corresponds with spectral and HVSR curves in* ***b)***, ***c)***, ***d)***, *and* ***e)***. ***b)***, ***c)***, ***d)*** *Fourier amplitude spectra in vertical, north and east components. The solid black line is the average of the spectra and the dashed line is the standard deviation.* ***e)*** *Horizontal-to-vertical spectral ratio (HVSR) curve; the vertical grey bar indicates the estimated fundamental frequency (f_0), where the thickness of the grey bar is the bounding error. The lighter grey band indicates the negative error, and the darker grey band positive error.*

Rayleigh wave signals from ambient seismic noise recordings (Aki, 1957; Wathelet et al., 2008; Molnar et al., 2010; Gosselin et al., 2018). In this study, we use frequency-wavenumber (f-k) processing to measure the phase velocity of Rayleigh waves at many frequencies (Lacoss et al., 1969). This technique requires synchronous recordings from instruments deployed in a 2D array (Fig. 2) because the propagation direction of background seismic signals is unknown and must be measured as part of the processing. All passive seismic recordings include three components; however, only vertical-component recordings are considered in this preliminary work because we can assume these are dominated by Rayleigh waves. The synchronous recordings are windowed according to the frequency (f) of interest. For each time window in f-k processing, the coherence of the Rayleigh wave signal across the array is estimated for various phase velocities and propagation directions (for the desired frequency band). This requires shifting individual windowed recordings in time based on a given wavenumber vector $\boldsymbol{k} = (k_x, k_y)$ and mapping the combined signal coherence on a 2D wavenumber grid. The location of maximum signal coherence on this wavenumber grid provides a single measurement of Rayleigh wave phase velocity (c) and propagation direction (θ) according to

$$c = \frac{2\pi f}{|\boldsymbol{k}|} \tag{2}$$

and

$$\theta = \arctan\left(\frac{k_x}{k_y}\right) \tag{3}$$

Each time window represents a single sample (estimates of c and θ). The ensemble of samples for all time windows, and across all frequencies, is considered to determine the dispersion curve (Fig. 4). We apply *f-k* processing to measure dispersion at 100 logarithmically spaced frequencies between 1 and 15 Hz; however, the actual frequency band over which dispersion can be measured is determined by the resolution and aliasing limits of the 2D array of the seismic instruments (Wathelet *et al.*, 2008). The resolution and aliasing limits are functions of the distance between instruments and their geometries. The resolution limit defines the ability of a particular seismic array to distinguish waves propagating at similar wavenumbers (*i.e.*, distinguish peaks on the wavenumber grid). Aliasing limits occur due to finite, discrete spatial sampling of the seismic wavefield. This introduces recurring peaks (side lobes) in the measured wavenumber grid, which can be summed incorrectly when determining signal coherence (Wathelet *et al.*, 2008, 2020). The use of several instrument spacing distances (Fig. 2a, b) enables wider resolution and aliasing limits (*i.e.*, wider frequency band). Although these limits are defined in terms of wavenumbers, they correspond to a frequency band of approximately 2–10 Hz for most array deployments in this study. Distributions of measured phase velocities at each frequency are often asymmetrical and contain outliers (Fig. 4); therefore, the dispersion curve is taken as the median phase velocity across the relevant frequency band. In this study, *f-k* processing for dispersion measurement was performed using Geopsy software (Wathelet *et al.*, 2020).

Preliminary soil shear-wave velocity inversion

Surface-wave dispersion data provide valuable constraints on soil V_S values, which are important for seismic hazard site classification and assessment. In this section, we present preliminary inferences of site soil properties based on measured dispersion data (see Surface-wave dispersion processing). Specifically, the dispersion data are inverted using a non-linear Bayesian methodology to estimate 1D models of site soil properties (Molnar *et al.*, 2010; Dettmer *et al.*, 2012; Gosselin *et al.*, 2017). Bayesian inversion is a probabilistic approach that considers the inversion solution as a probability density over model parameters (known as a posterior probability density). For simplicity, this preliminary paper assumes a two-layer model representative of unconsolidated sediment over bedrock. Furthermore, this paper assumes lateral heterogeneity over the array site, which may not be an accurate assumption at all sites (see Discussion for further details). Because this inversion problem is non-linear, we applied Markov-chain Monte Carlo sampling to generate an ensemble of model parameter combinations that agree with the data (Brooks *et al.*, 2011). The parameters of the model (layer V_S values and layer thicknesses) are restricted to geophysically realistic values; however, wide bounds are employed to ensure that the solution is primarily constrained by the dispersion data.

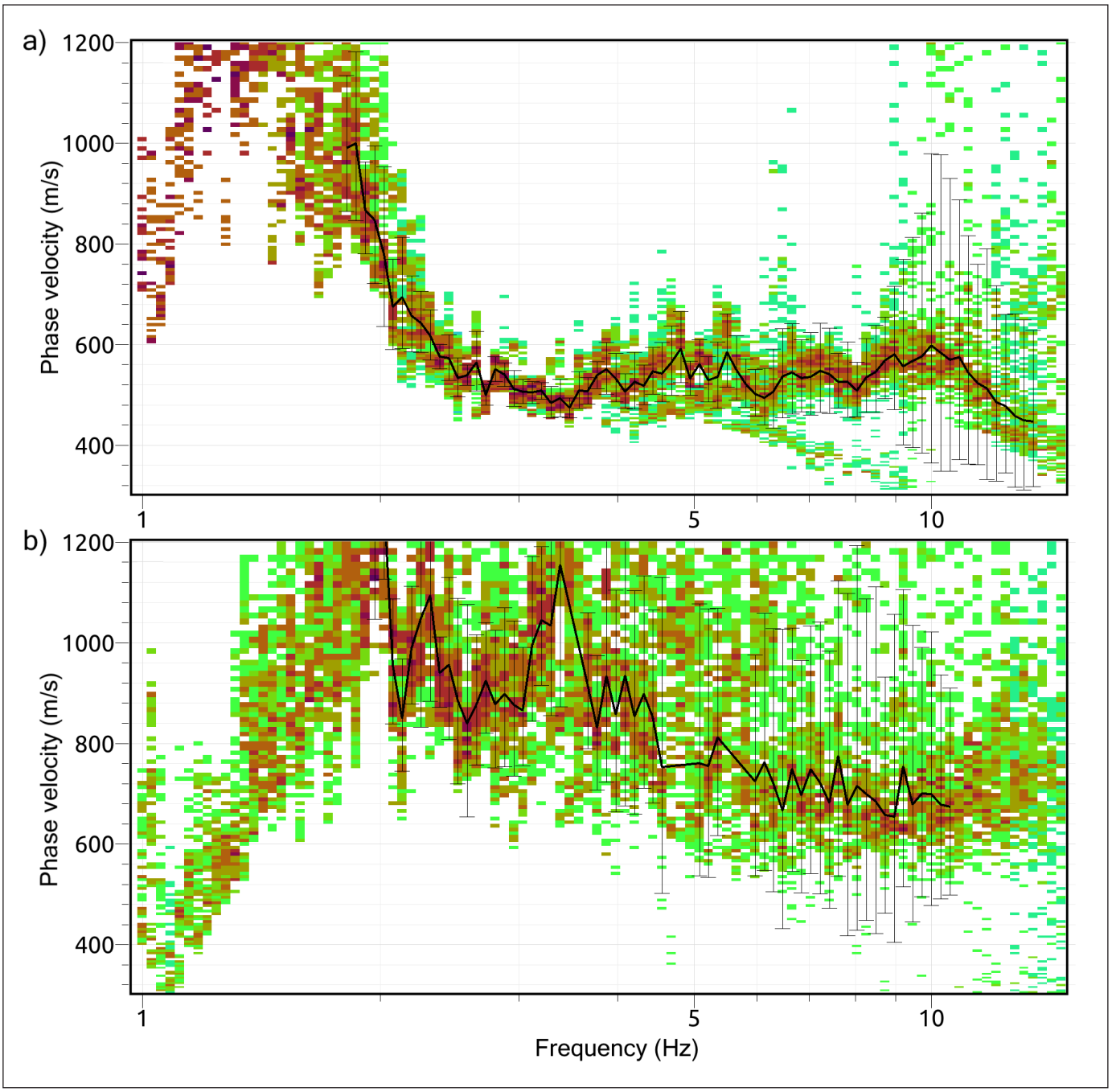

Figure 4. *Frequency-wavenumber processing of ambient seismic noise recordings at sites* **a)** *HJ05 and* **b)** *HJ11. The red and green bars represent high and low probability, respectively. Black lines illustrate the selected dispersion data. The histograms for HJ05 and HJ11 illustrate high and low-quality examples of frequency-wavenumber processing, respectively.*

Figure 5 illustrates estimated V_S as a function of depth at sites HJ05 and HJ11. The V_S estimates are presented as probability densities as a function of depth, where light colours indicate high probability. We observed that sediment velocities are generally lower at HJ05 than at HJ11. This is expected, given the difference in measured dispersion data (Fig. 4), which show that high-frequency (*i.e.*, shallow depth), surface-wave velocities are much higher at HJ11. Resolution in geophysical inversions typically degrades with increasing depth. Our results exhibit higher uncertainty in V_S at greater depths (Fig. 5). We also present

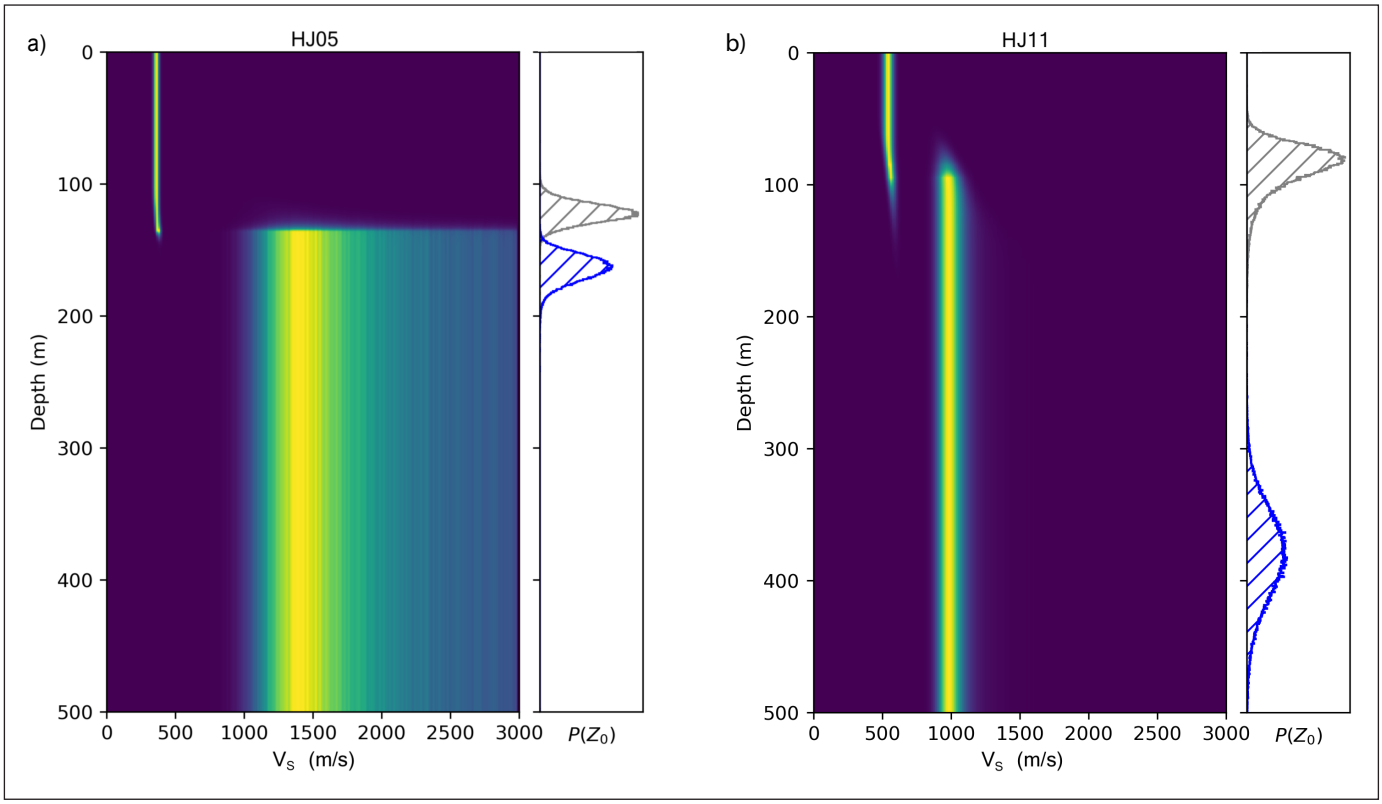

Figure 5. *Results for simple two-layer probabilistic inversions at sites* ***a)*** *HJ05, and* ***b)*** *HJ11. Depth marginal probability distributions of inferred shear-wave velocities (V_S) are shown, with yellow and blue representing high and low probability, respectively. Marginal probability distributions for inferred layer thickness (interface depth; $P(Z_0)$) are shown in grey. The probability distribution of the inferred seismic impedance contrasts associated with f_0 in horizontal-to-vertical spectral ratio curves is shown in blue. Note that the distribution for depth is outside of the plot bounds for HJ11.*

marginal distributions of the thickness of the surficial layer, which can be interpreted as depth to bedrock; however, as will be discussed below, this assumption may not be true for all sites. Figure 6 illustrates the fit between measured and predicted surface-wave dispersion data. The measured data are those shown in Figure 4 (sites HJ05 and HJ11), whereas the predicted data represent a numerical simulation corresponding with a given inversion solution. Some complexities in the measured dispersion data are not fit by this simple, two-layer case (e.g., high-frequency data for site HJ05). This is expected given the simplicity of the model used in this preliminary analysis.

Discussion

Horizontal-to-vertical spectral ratio results

Fundamental frequencies were identified at each of the 23 measured sites and are summarized in Appendix A. Nine sites measured using the Tromino seismometer were excluded from these results due to poor recording quality, insufficient recording duration, complex geological site conditions, or a combination of these factors. Fundamental frequencies identified at sites recorded using Tromino seismometers and sensor arrays are illustrated in Figures 3e and 7, respectively. Fundamental frequencies identified throughout the study area range from 0.3 to 0.8 Hz, indicating that a thick layer of soft sediment overlies bedrock in the area (Nakamura, 2000). This suggests a potential for amplified shaking due to resonance effects caused by the significant velocity contrast between the bedrock layer and overlying sediment (Hunter and Crow, 2015). Figures 3e and 7d show HVSR results from co-located Tromino (site TR15) and array (site HJ11) recordings south of central Haines Junction (see Fig. 1 for site locations). The HVSR curves representative of this site demonstrate that both sensor types and calculations produce consistent results with a fundamental

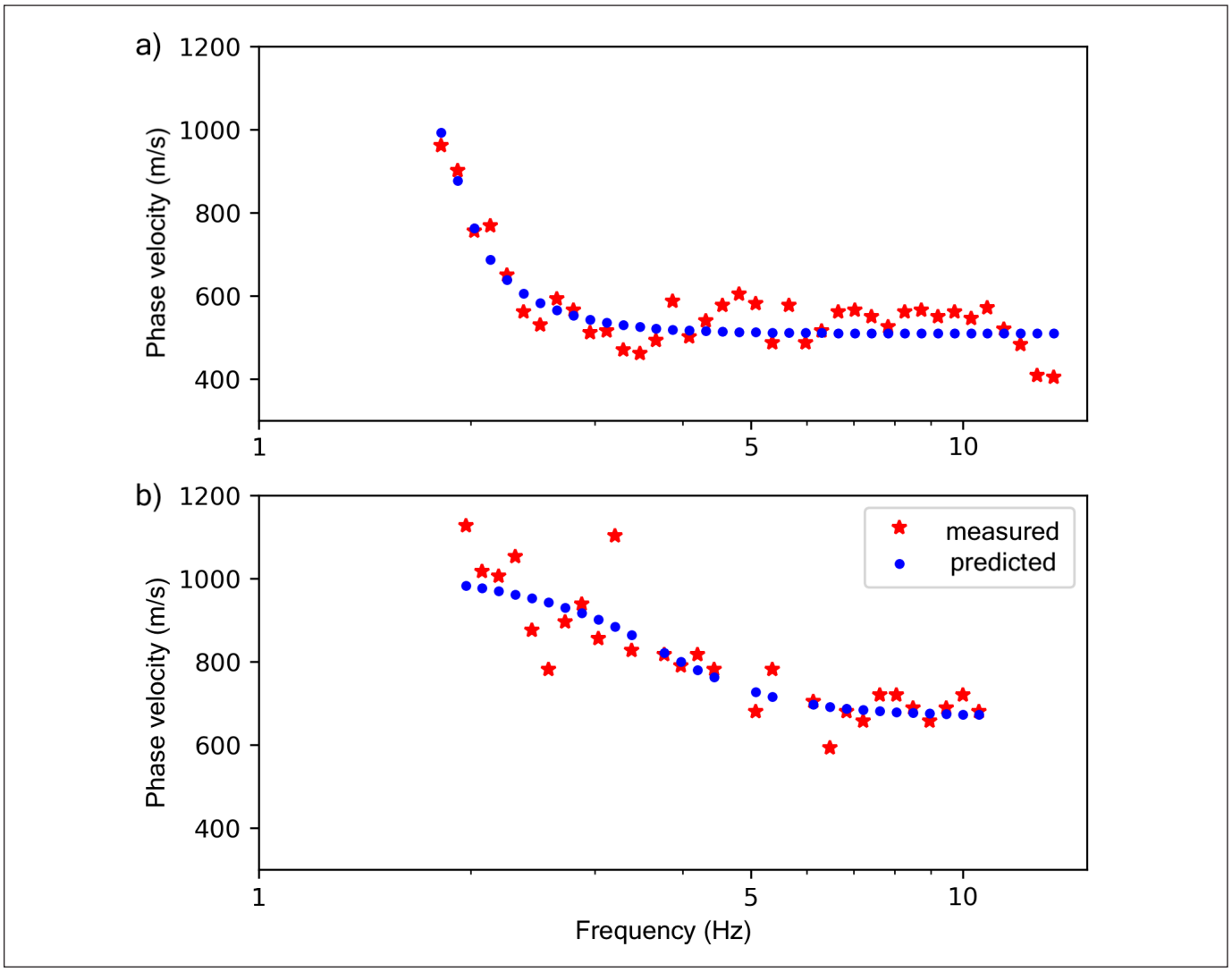

Figure 6. *Comparison of measured and predicted dispersion data for sites* ***a)*** *HJ05, and* ***b)*** *HJ11. Measured dispersion data are the same as shown in Figure 4. Predicted dispersion data are simulated using the solutions from the simplified two-layer probabilistic inversions.*

frequency of approximately 0.4 Hz and amplitude of approximately 4 to 5. Overall, average HVSR curves calculated from multiple sensors have a broader f_0 peak compared to single-station Tromino sites (see averaged HVSR curves in Fig. 7). This is likely due to instrumentation, seismic noise and lateral heterogeneity effects, which cause discrepancies between HVSR results from different sensors at a given array site. The multiple, narrow, shifted peaks seen in the stacked f_0 peaks identified at site HJ11 (Fig. 7c) suggest the sloped site has laterally varying subsurface geology over a scale of hundreds of metres (Molnar et *al*., 2022). Site HJ05 is located north of Haines Junction and has a higher fundamental frequency compared to the HJ11/TR15 site, south of Haines Junction. This difference in HVSR suggests that subsurface geology varies laterally over larger scales throughout the area.

Most sites demonstrate at least one high-frequency peak of 10–50 Hz (Appendix A). Additional peaks in HVSR curves are indicative of additional discrete sediment layering in the overburden between the surface and bedrock layer (Mihaylov et *al*., 2016). Because peak frequency values are inversely proportional to layer boundary depth (Nakamura, 2000), depth of the fundamental frequency can be estimated by dividing the V_S of the uppermost layer by the measured quarter-wavelength. Assuming the minimum V_S is approximately 250 m/s in the uppermost layer, peaks identified at high frequencies of approximately 25 Hz

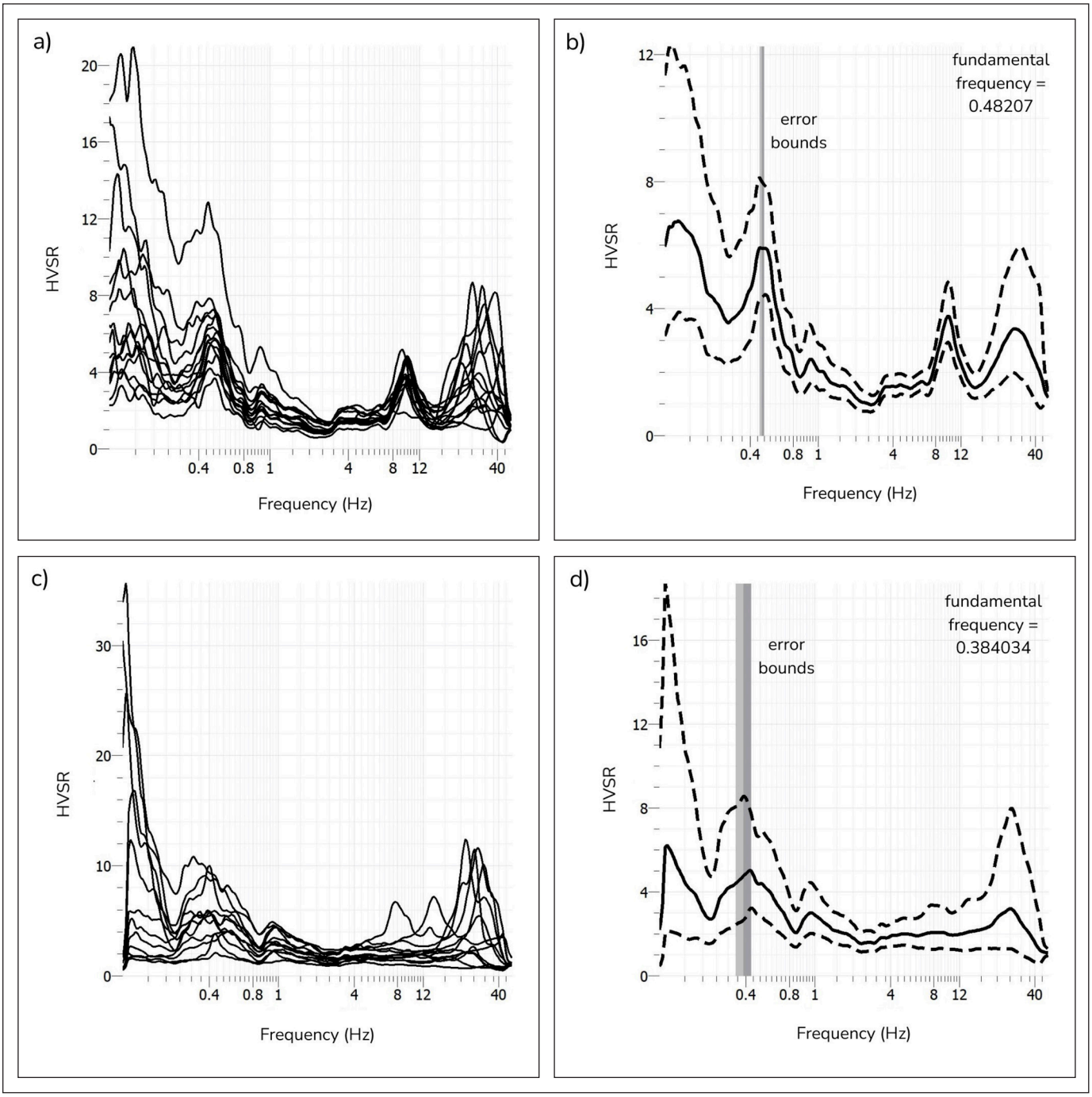

Figure 7. *Summarized and averaged horizontal-to-vertical spectral ratio (HVSR) curves from all sensors at array sites* **a**, **b)** *HJ05, and* **c**, **d)** *HJ11.* **a)** *and* **c)** *show stacked average HVSR curves calculated from each individual sensor recording.* **b)** *and* **d)** *show the average (solid line) and one standard deviation (dashed lines) HVSR curve for each site. Grey vertical error bars show the standard deviation of the average fundamental frequency. Sensors that produced anomalous HVSR curves were excluded, as indicated in Appendix A1.*

for sites HJ05, HJ11 and TR15 (Figs. 3e, 7) indicate sediment layering to be as shallow as approximately 2.5 m below the surface. Secondary or tertiary peaks identified at lower frequencies, for example, at approximately 9.5 Hz at site HJ05 (Fig. 7b), indicate that the interface of intermediate soil layers extends deeper into the subsurface, to 6–12 m deep.

The frequency, amplitude and number of high-frequency peaks vary among the studied sites (see Appendix A), suggesting complex sediment layering structure in the overburden that varies laterally. The multiple peaks at approximately 25 Hz, which shifted in frequency depending on the instrument (Fig. 7a, c), suggest that near-surface intermediate soil layers vary over the 120 m lateral extent of the array site (Molnar et al., 2022). Higher frequency peaks, consequently, are not well constrained at these sites. In comparison, the lower frequency secondary peak at site HJ05 (Fig. 7a, b) has a very similar frequency value (approximately 9.5 Hz) for almost all sensors, indicating that the boundary depth of this layer is more homogeneous across the site. Because permafrost is present but discontinuous throughout the Haines Junction region (Rampton and Paradis, 1979), it is possible that distinct overburden layers found at many of the measured sites are representative of an active permafrost layer. For example, the subsurface geology identified by HVSR results at site HJ05 (*i.e.*, two distinct shallow layers) is consistent with nearby electrical resistivity tomography (ERT) conducted by YGS (P. Lipovsky, pers. comm., 2021) and may indicate the presence of a seasonally active shallow soil structure. Permafrost at HJ05 is likely discontinuous and degrading given the alterations to surficial vegetation cover (HJ05 is an agricultural field). In contrast, site HJ11 is in a wooded area on a gently sloping, north-facing incline with nearby geomorphological signatures of permafrost processes. It is difficult, however, to determine whether high-frequency peaks identified at many sites are produced by a discrete permafrost layer or other geological factors without additional data and/or seasonal monitoring.

Dispersion curve inversion results

As expected from inversion of surface-wave dispersion data, with an increase in depth, V_S generally increases, as does uncertainty in V_S profiles, and the estimated transition depth to bedrock is resolved. What is most reliable is the average V_S constrained over the depth extent corresponding with the depth resolution capabilities of the array configuration used in this study. Average surficial sediment velocities and thicknesses with associated uncertainties, inferred from surface-wave dispersion data, are summarized in Appendix B for all array sites. The maximum depth resolution is a function of array geometry, which defines the low-frequency dispersion that can be measured (see Surface-wave dispersion processing). The depth resolution limit is also a function of geological conditions (soil V_S), which define the wavelength of these low-frequency seismic waves. The depth resolution limit is typically the maximum station separation distance (Park *et al.*, 1999; Wathelet *et al.*, 2008). This is 120 m for most sites considered in this study.

The wavelength limitations in HVSR measurements are defined by the recording parameters of the AV measurements (*e.g.*, length of recording) and the sensitivity of the instrument (*e.g.*, broadband or high frequency). In this study, HVSR measurements provide information over a significantly wider frequency band (0.1–50 Hz) compared to the measured dispersion; however, HVSR suffers from solution non-uniqueness between soil V_S and depth to impedance contrasts. To test the consistency between our simplified inversion results and HVSR observations, we calculated the depth associated with the f_0 peaks using sediment V_S values inferred from surface-wave dispersion. Uncertainties in both f_0 peaks and inferred V_S are propagated through this analysis; these depth estimates are summarized in Appendix B. Examples of this analysis are illustrated by the blue histogram in Figure 5a and b. At HJ05, the depth to bedrock inferred from the inversion is in relatively good agreement with the depth estimated from the f_0 peak. The discrepancy between the two distributions is likely attributed to the simplified velocity structure assumed for the inversion method. Alternatively, the discrepancy between bedrock depth estimates may be attributed to the simple quarter-wavelength assumption for HVSR measurements and the effects of high-frequency HVSR peaks (which are not considered in this simple analysis). At HJ11, the depth to bedrock estimated using the f_0 peak is much deeper than the interface inferred from dispersion data (approximately 380 ± 36 m). This suggests that the interface resolved in the inversion of dispersion data is not bedrock depth. Instead, this layer likely represents either a discrete intermediate sediment layer or a gradual increase in sediment V_S with increasing depth. This would also

explain why the distribution of V_S values in the deeper layer is much lower at HJ11 compared to HJ05 (Fig. 5). Future work will estimate more robust models of V_S structure by jointly inverting dispersion and HVSR data, and consider more complex models of soil-layering structure.

Regional observations

The average fundamental frequencies (f_0) for all single-station and array sites are mapped in Figure 8 to demonstrate site stiffness and/or sediment thickness as they vary spatially throughout the Haines Junction region. Eight sites in the south of our study area, including the colocated HJ11 array and TR15 single-station sites, demonstrate fundamental frequencies below 0.5 Hz. Meanwhile, eight sites in the north of our study area exhibit frequencies 0.5 Hz and above. These observations suggest a shallower depth to bedrock, and/or stiffer (*i.e.*, higher seismic velocities) sediments, in the north of our study area compared with the south. The regional observations in HVSR fundamental frequencies are consistent with our interpretation of the inverted surface-wave dispersion curve results; however, dispersion data suggest higher sediment velocities in the south of our study area compared with the north (Fig. 5), as well as high variability in sediment V_S across the study area (see Appendix B). Interpreted together, these data imply that regional trends in measured f_0 are likely attributed to bedrock depth rather than site soil V_S properties. A possible explanation for deeper soft soil layers at southern sites is their proximity to the Dezadeash River running through central Haines Junction, which is associated with a sediment-filled river valley and associated basin in the subsurface. In comparison, northern sites in our

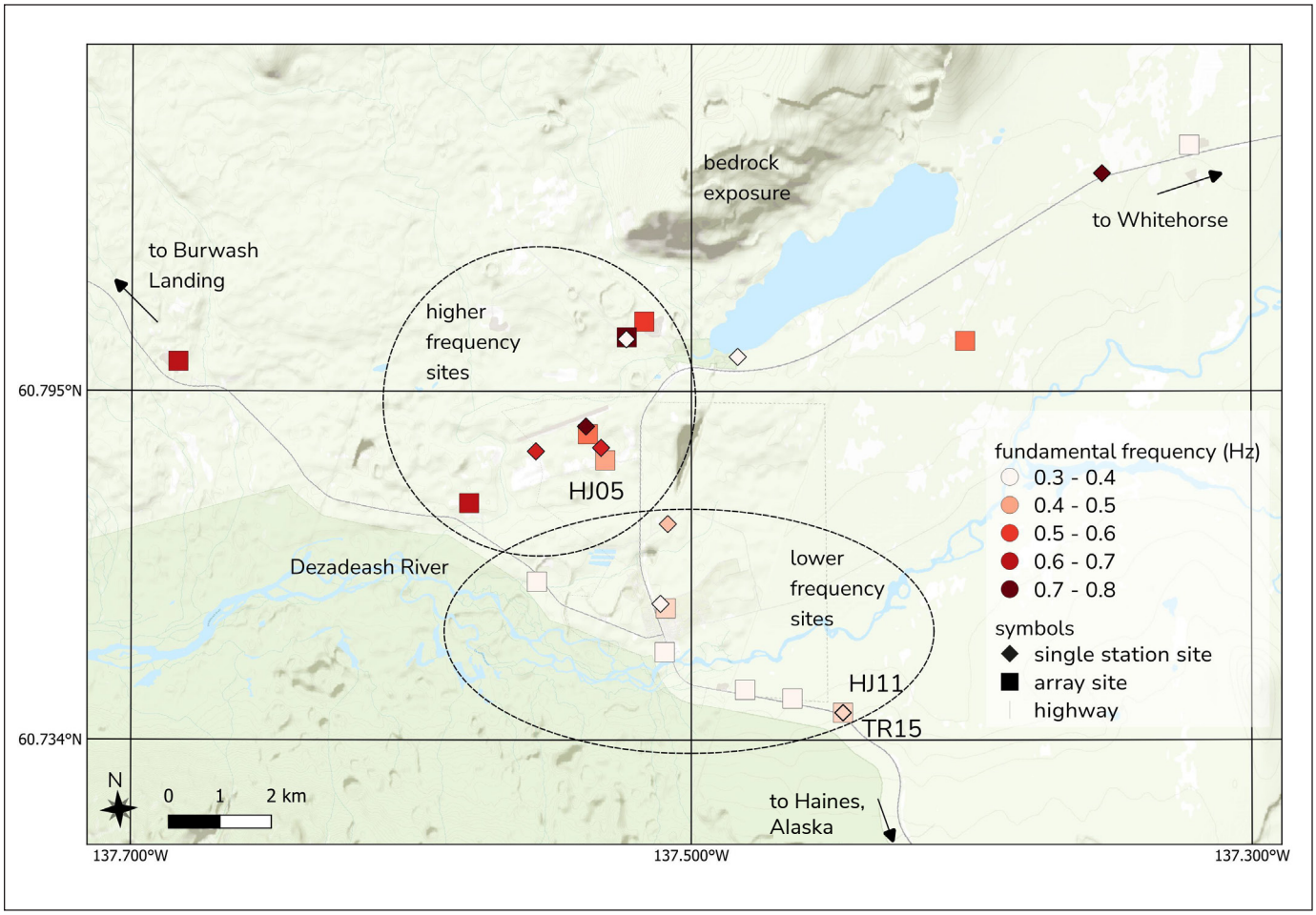

Figure 8. *Map of site locations in the Haines Junction area with identified fundamental frequencies from horizontal-to-vertical spectral ratio analysis. Labelled sites HJ05, HJ11 and TR15 are discussed in the text. Areas with relatively low (south) and high (north) fundamental frequencies are identified.*

study area are proximal to bedrock exposure (area of high topographic relief shown at the northern extent of our study region in Figs. 1 and 8). Proximity to bedrock supports our interpretation of a shallower depth to the sediment–bedrock interface. Sites located outside of these two subregions (circled in Fig. 8) exhibit varying fundamental frequencies, demonstrating the overall complexity in subsurface geology throughout the study area (Rampton and Paradis, 1979; Israel *et al*., 2017). They may also demonstrate site-specific hydrogeological and cryospheric processes.

Generally, sites with softer soils experience more amplified ground shaking during an earthquake compared to stiffer sediments or hardrock (Hunter and Crow, 2015). We do not comment on seismic hazard associated with regionally variable soil stiffness properties in this preliminary paper; however, site components of seismic hazard may also be attributed to subsurface basin structures that can significantly amplify and extend the duration of earthquake shaking (Bard and Bouchon, 1985). It is likely that central and south Haines Junction are at increased seismic hazard due to the presence of subsurface basin structures in the region.

Conclusion

Southwestern Yukon has abundant seismicity and complex active tectonics, and communities in the region are at risk of earthquake-associated hazards including shaking amplification and resonance. Although seismic hazard is elevated in southwestern Yukon, the contributions of local site effects to the overall hazard (within Canada's national hazard model) are largely unknown. To address this knowledge gap, preliminary site characterization was completed in the Haines Junction area using ambient vibration techniques. Passive seismic recordings were taken at 23 sites, including 9 single-station sites and 14 multi-instrument array sites. Time series recordings were processed to determine HVSR curves for all sites. Fundamental frequencies ranging from 0.3 to 0.8 Hz were readily identified; these values suggest regional variability in soil seismic properties, sediment depths and associated site-specific seismic hazards. Recordings from array sites were used to measure surface-wave dispersion, which was subsequently used to infer shallow soil V_S properties. When depth to bedrock is within array depth resolution limits, inversion results are generally in agreement with HVSR observations.

Discrepancies between the results obtained from the two seismic data types may be due to lateral soil heterogeneity at sites, resolution limitations due to array aperture, the assumptions of the simplified (two-layer) inversion model, the simple quarter-wavelength assumption for HVSR measurements, and the effects of multiple HVSR peaks (which were not considered in this simple analysis). This paper provides preliminary site characterizations and mapping to identify local site effects and better understand seismic hazard in Haines Junction, Yukon. Future work will involve joint inversion of HVSR and measured surface-wave dispersion to obtain more robust V_S depth profiles, which will enable more complete site characterization, including seismic site classification, and amplification and resonance modelling.

Acknowledgments

We respectfully acknowledge that data for this study were recorded on the Traditional Territory of the Champagne and Aishihik First Nations. This work is partially supported by Natural Resources Canada (NRCan) through a research contract to Tess Leishman. The Natural Science and Engineering Research Council (Canada) supports this work through a postdoctoral fellowship (Jeremy M. Gosselin) and Discovery grants (Jan Dettmer, John Cassidy and Stan Dosso). Data were processed using Geopsy software (Wathelet et al., 2020). We thank the Yukon Geological Survey for providing funding as well as local geological knowledge and ERT survey results to guide the selection of site location. We thank Youngjun Jeon, Min-Hyug Koh and Minog Kim for their valuable assistance collecting the passive seismic data discussed in this paper; Andrew Schaeffer for help accessing instrumentation; Panya Lipovsky for useful insights on local geology; and Derek Cronmiller for helpful comments on this manuscript. Finally, we thank Camille Brillon for a critical review that improved this paper.

Tabulated HVSR and dispersion values are available in Appendices A and B. This is NRCan contribution number 20230333.

References

Adams, J., Allen, T., Halchuk, S. and Kolaj, M., 2019. Canada's 6th generation seismic hazard model, as prepared for the 2020 National Building Code of Canada. *In*: 12th Canadian Conference on Earthquake Engineering, Canadian Association for Earthquake Engineering, paper 192-Mkvp-139, 8 p.

Aki, K., 1957. Space and time spectra of stationary stochastic waves, with special reference to microtremors. Bulletin of the Earthquake Research Institute, vol. 35, p. 415–456.

Allen, T., Adams, J., Halchuk, S. and Rogers, G., 2015. 5th generation seismic hazard model for north-western Canada. *In*: The 11th Canadian Conference on Earthquake Engineering, Canadian Association for Earthquake Engineering, paper 93782, 13 p.

Bard, P.Y. and Bouchon, M., 1985. The two-dimensional resonance of sediment-filled valleys. Bulletin of the Seismological Society of America, vol. 75, no. 2, p. 519–541. https://doi.org/10.1785/BSSA0750020519.

Biegel, K., Gosselin, J. and Dettmer, J., 2023. Preliminary double-difference relocation earthquake catalogue for southwestern Yukon centred along the Denali fault zone. *In*: Yukon Exploration and Geology 2022, K.E. MacFarlane (ed.), Yukon Geological Survey, p. 1–18, plus digital appendices.

Brooks, S., Gelman, A., Jones, G. and Meng, X.L. (eds.), 2011. Handbook of Markov Chain Monte Carlo (1st ed.). Chapman and Hall/CRC, New York, 619 p. https://doi.org/10.1201/b10905.

Bruhn, R.L., Sauber, J., Cotton, M.M., Pavlis, T.L., Burgess, E., Ruppert, N. and Forster, R.R., 2012. Plate margin deformation and active tectonics along the northern edge of the Yakutat terrane in the Saint Elias orogen, Alaska, and Yukon, Canada. Geosphere, vol. 8, no. 6, p. 1384–1407. https://doi.org/10.1130/GES00807.1

Clague, J.J. and Rampton, V.N., 1982. Neoglacial Lake Alsek. Canadian Journal of Earth Sciences, vol. 19, no. 1, p. 94–117. https://doi.org/10.1139/e82-008

Dettmer, J., Molnar, S., Steininger, G., Dosso, S.E. and Cassidy, J.F., 2012. Trans-dimensional inversion of microtremor array dispersion data with hierarchical autoregressive error models. Geophysical Journal International, vol. 188, no. 2, p. 719–734. https://doi.org/10.1111/j.1365-246X.2011.05302.x

Doser, D.I. and Rodriguez, H., 2011. A seismotectonic study of the southeastern Alaska region. Tectonophysics, vol. 497, no. 1–4, p. 105–113. https://doi.org/10.1016/j.tecto.2010.10.019

Enkelmann, E., Zeitler, P.K., Pavlis, T.L., Garver, J.I. and Ridgway, K.D., 2009. Intense localized rock uplift and erosion in the St Elias orogen of Alaska. Nature Geoscience, vol. 2, no. 5, p. 360–363. https://doi.org/10.1038/ngeo502

Frigo, M. and Johnson, S., 2005. The design and implementation of FFTW3. *In*: Proceedings of the IEEE, vol. 93, no. 2, p. 216–231. https://doi.org/10.1109/JPROC.2004.840301

Gosselin, J.M., Cassidy, J.F., Dosso, S.E. and Brillon, C., 2018. Probabilistic seismic-hazard site assessment in Kitimat, British Columbia, from Bayesian inversion of surface-wave dispersion. Canadian Geotechnical Journal, vol. 55, no. 7, p. 928–940. https://doi.org/10.1139/cgj-2017-0265

Gosselin, J.M., Dosso, S.E., Askan, A., Wathelet, M., Savvaidis, A. and Cassidy, J.F., 2022. A review of inverse methods in seismic site characterization. Journal of Seismology, vol. 26, no. 4, p. 781–821. https://doi.org/10.1007/s10950-021-10047-8

Gosselin, J.M., Dosso, S.E., Cassidy, J.F., Quijano, J.E., Molnar, S. and Dettmer, J., 2017. A gradient-based model parametrization using Bernstein polynomials in Bayesian inversion of surface wave dispersion. Geophysical Journal International, vol. 211, no. 1, p. 528–540. https://doi.org/10.1093/gji/ggx323

Government of Yukon, 2002. Haines junction borehole logging report. Water Resources Branch, Water Well Registry Open File 10337404. https://ftp-env-public.gov.yk.ca/WR/YWWR/101130001.pdf, [accessed December 2023].

Hunter, J.A. and Crow, H.L. (eds.), 2015. Shear wave velocity measurement guidelines for Canadian seismic site characterization in soil and rock. Geological Survey of Canada, General Information Product 110e, 226 p.

Israel, S., Friend, M. and Borch, A., 2017. Preliminary report on the bedrock geology of the Long Lake and Moraine Lake areas, southwestern Yukon (NTS 115A/15 and 115H/2 and 7). *In*: Yukon Exploration and Geology 2016, K.E. MacFarlane and L.H. Weston (eds.), Yukon Geological Survey, p. 87–102.

Kolaj, M., Adams, J. and Halchuk, S., 2020. The 6th generation seismic hazard model of Canada. *In*: The 17th World Conference on Earthquake Engineering, Sendai, Japan, Paper 1c-0028, 12 p.

Kreemer, C., Blewitt, G. and Klein, E.C., 2014. A geodetic plate motion and global strain rate model. Geochemistry, Geophysics, Geosystems, vol. 15, no. 10, p. 3849–3889. https://doi.org/10.1002/2014GC005407

Lacoss, R.T., Kelly, E.J. and Toksöz, M.N., 1969. Estimation of seismic noise structure using arrays. Geophysics, vol., 34, no. 1, p. 21–38. https://doi.org/10.1190/1.1439995

Lamontagne, M. and Bent, A.L., 2021. Earthquakes in the eastern Canadian Arctic: Past occurrences, present hazard, and future risk. Seismological Research Letters, vol. 92, no. 5, p. 2824–2837. https://doi.org/10.1785/0220210014

Meighan, L.N., Cassidy, J.F., Mazzotti, S. and Pavlis, G.L., 2013. Microseismicity and tectonics of southwest Yukon Territory, Canada, using a local dense seismic array. Bulletin of the Seismological Society of America, vol. 103, no. 6, p. 3341–3346. https://doi.org/10.1785/0120130068

Mihaylov, E.I., Naggar, M.H. and Dineva, S., 2016. Separation of high- and low-level ambient noise for HVSR: Application in city conditions for Greater Toronto Area. Bulletin of the Seismological Society of America, vol. 106, no. 5, p. 2177–2184. https://doi.org/10.1785/0120150389

Molnar, S., Dosso, S.E. and Cassidy, J.F., 2010. Bayesian inversion of microtremor array dispersion data in southwestern British Columbia. Geophysical Journal International, vol. 183, issue 2, p. 923–940. https://doi.org/10.1111/j.1365-246X.2010.04761.x

Molnar, S., Sirohey, A., Assaf, J., Bard, P.-Y., Castellaro, S., Cornou, C., Cox, B., Guillier, B., Hassani, B., Kawase, H., Matsushima, S., Sánchez-Sesma, F.J. and Yong, A., 2022. A review of the microtremor horizontal-to-vertical spectral ration (MHVSR) method. Journal of Seismology, vol. 26, no. 4. p. 653–685. https://doi.org/10.1007/s10950-021-10062-9

Nakamura, Y., 1989. A method for dynamic characteristics estimation of subsurface using microtremor on the ground surface. Quarterly Report of Railway Technical Research Institute, vol. 30, issue 1, p. 25–33.

Nakamura, Y., 2000. Clear identification of fundamental idea of Nakamura's technique and its applications. *In*: Proceedings of the 12th World Conference on Earthquake Engineering, Auckland, New Zealand. Paper no. 2656.

Nelson, J.L., Colpron, M. and Israel, S., 2013. The Cordillera of British Columbia, Yukon, and Alaska: Tectonics and metallogeny. *In*: Tectonics, Metallogeny, and Discovery: The North American Cordillera and Similar Accretionary Settings, M. Colpron, T. Bissig, B.G. Rusk, and J.F.H. Thompson (eds.), Society of Economic Geologists Special Publication, vol. 17, p. 53–109. https://doi.org/10.5382/SP.17.03

Park, C.B., Miller, R.D. and Xia, J., 1999. Multichannel analysis of surface waves. Geophysics, vol. 64, no. 3, p. 800–808. https://doi.org/10.1190/1.1444590

Rampton, V.N. and Paradis, S., 1979. Surficial geology and geomorphology, Pine Lake, Yukon Territory. Geological Survey of Canada, Open File Preliminary Map 16–1981, 1 sheet. https://doi.org/10.4095/119387

SESAME, 2004. Guidelines for the Implementation of the H/V Spectral Ratio Technique on Ambient Vibrations: Measurements, Processing and Interpretation. SESAME European Research Project WP12 - Deliverable D23.12, European Commission – Research General Directorate Project No. EVG1-CT-2000-00026 SESAME, 62 p.

Shapiro, N.M. and Campillo, M., 2004. Emergence of broadband Rayleigh waves from correlations of the ambient seismic noise. Geophysical Research Letters, vol. 31, no. 7, article L07614, 4 p., https://doi.org/10.1029/2004GL019491

Turner, D.G., Ward, B.C., Froese, D.G., Lamothe, M., Bond, J.D. and Bigelow, N.H., 2016. Stratigraphy of Pleistocene glaciations in the St Elias Mountains, southwest Yukon, Canada. Boreas, vol. 45, no. 3, p. 521–536. https://doi.org/10.1111/bor.12172

Wathelet, M., Chatelain, J.L., Cornou, C., Di Giulio, G., Guillier, B., Ohrnberger, M. and Savvaidis, A., 2020. Geopsy: A user-friendly open-source tool set for ambient vibration processing. Seismological Research Letters, vol. 91, no. 3, p. 1878–1889.

Wathelet, M., Jongmans, D., Ohrnberger, M. and Bonnefoy-Claudet, S., 2008. Array performances for ambient vibrations on a shallow structure and consequences over V_S inversion. Journal of Seismology, vol. 12, p. 1–19. https://doi.org/10.1007/s10950-007-9067-x

Yukon Geological Survey, 2020. A digital atlas of terranes for the northern Cordillera. Yukon Geological Survey, http://data.geology.gov.yk.ca/Compilation/2, [accessed November 20, 2023].

Appendix A

Average fundamental peak frequency (f_0) and higher order frequency peak (f_1) values for ambient vibration data collected from 23 sites (14 sensor arrays [HJ stations] and 9 single-sensor sites [TR stations]) in the Haines Junction area, Yukon. Error bounds are one standard deviation from the identified peak. F_1 peak error bounds are calculated for TR stations only.

Site name	Latitude WGS84 EPSG:4326	Longitude WGS84 EPSG:4326	F_0 peak (Hz)	F_0 peak error bounds (Hz)	F_0 amplitude, A_0	F_1 peak (Hz)	F_1 peak error bounds (Hz)	F_1 amplitude, A_1	Multiple high frequency peaks?
HJ01	60°50'17.02"N	137°19'18.78"W	0.35933	0.31622, 0.378437	4.51	42.686	–	2.32	no
HJ02	60°48'13.71"N	137°24'7.81"W	0.521971	0.504724, 0.539808	4.67	15.848	–	3.18	no
HJ03	60°48'25.91"N	137°31'0.80"W	0.599041	0.518735, 0.691779	8	40.762	–	4	no
HJ04	60°48'16.08"N	137°31'23.29"W	0.813822	0.657624, 1.00712	4.54	7.773	–	2.44	yes
HJ05	60°46'58.52"N	137°31'50.87"W	0.48207	0.465833, 0.498872	5.93	9.64	–	3.76	yes
HJ06	60°47'14.99"N	137°32'13.20"W	0.496907	0.471199, 0.524017	5.69	14.9616	–	2.12	uncertain
HJ07	60°45'25.43"N	137°30'32.95"W	0.38164	0.366159, 0.397776	5.67	14.191	–	2.47	no
HJ08	60°48'0.68"N	137°41'0.28"W	0.648612	0.618004, 0.680735	3.64	42.3887	–	3.46	no
HJ09	60°44'28.63"N	137°27'50.19"W	0.366304	0.333607, 0.402206	3.23	8.115	–	2.11	yes
HJ10	60°44'34.11"N	137°28'50.89"W	0.330034	0.290675, 0.374722	3.78	21.5663	–	2.88	no
HJ11	60°44'19.64"N	137°26'45.13"W	0.384301	0.339873, 0.434536	4.76	26.4391	–	3.26	no
HJ12	60°45'42.10"N	137°33'18.50"W	0.319797	0.302239, 0.338376	4.15	22.6249	–	3.07	no
HJ13	60°44'57.74"N	137°30'34.25"W	0.335154	0.31309, 0.358773	5.28	10.25	–	2.86	yes
HJ14	60°46'31.55"N	137°34'45.88"W	0.629003	0.581476, 0.680414	9.36	26.8211	–	4.27	uncertain

Average fundamental peak frequency (f_0) and higher order frequency peak (f_1) values for ambient vibration data collected from 23 sites (14 sensor arrays [HJ stations] and 9 single-sensor sites [TR stations]) in the Haines Junction area, Yukon. Error bounds are one standard deviation from the identified peak. F_1 peak error bounds are calculated for TR stations only. (continued)

Site name	Latitude WGS84 EPSG:4326	Longitude WGS84 EPSG:4326	F_0 peak (Hz)	F_0 peak error bounds (Hz)	F_0 amplitude, A_0	F_1 peak (Hz)	F_1 peak error bounds (Hz)	F_1 amplitude, A_1	Multiple high frequency peaks?
TR02	60°49'59.16"N	137°21'11.25"W	0.614592	0.505822, 0.746751	1.60	15.446	14.3309 and 16.6479	2.37	yes
TR05	60°48'14.85"N	137°31'23.81"W	0.290344	0.270237, 0.311947	8.88	28.9748	28.1074 and 29.869	2.76	no
TR07	60°47'6.41"N	137°31'56.23"W	0.596518	0.518478, 0.686306	2.53	none	n/a	n/a	n/a
TR08	60°48'3.67"N	137°29'0.48"W	0.29043	0.261372, 0.322717	2.56	24.0057	20.639 and 27.9217	1.73	no
TR09	60°47'19.90"N	137°32'15.68"W	0.655948	0.527858, 0.815119	2.97	19.8421	18.042 and 21.8218	1.70	yes
TR10	60°47'4.15"N	137°33'20.06"W	0.552875	0.463679, 0.659231	4.84	52.1615	50.1881 and 54.2126	2.50	no
TR11	60°45'28.21"N	137°30'39.70"W	0.377057	0.338841, 0.419584	1.79	4.57387	4.33866 and 4.82183	4.38	yes
TR15	60°44'19.64"N	137°26'45.13"W	0.405334	0.354963, 0.462852	3.91	33.681	32.4124 and 34.9993	2.48	no
TR20	60°46'18.49"N	137°30'30.36"W	0.45779	0.424018, 0.494252	1.51	14.6759	14.2999 and 15.0617	4.17	no

Appendix B

Summarized results of surface-wave dispersion inversions for data collected at 14 multi-sensor array sites in the Haines Junction area, Yukon.

Site name	Latitude WGS84 EPSG:4326	Longitude WGS84 EPSG:4326	Depth to layer boundary (m) calculated from surface-wave dispersion	Sediment velocity (m/s)	Depth to layer boundary (m) calculated from f_0
HJ01	60°50'17.02"N	137°19'18.78"W	63 ± 2	213 ± 6	116 ± 4
HJ02	60°48'13.71"N	137°24'7.81"W	149 ± 9	346 ± 21	139 ± 9
HJ03	60°48'25.91"N	137°31'0.80"W	54 ± 4	331 ± 23	118 ± 8
HJ04	60°48'16.08"N	137°31'23.29"W	46 ± 3	113 ± 10	31 ± 3
HJ05	60°46'58.52"N	137°31'50.87"W	122 ± 8	382 ± 22	164 ± 10
HJ06	60°47'14.99"N	137°32'13.20"W	160 ± 10	400 ± 50	167 ± 21
HJ08	60°45'25.43"N	137°30'32.95"W	162 ± 19	484 ± 521	162 ± 176
HJ09	60°48'0.68"N	137°41'0.28"W	87 ± 12	377 ± 30	202 ± 17
HJ10	60°44'28.63"N	137°27'50.19"W	70 ± 4	452 ± 22	263 ± 15
HJ11	60°44'34.11"N	137°28'50.89"W	87 ± 17	738 ± 68	380 ± 36
HJ13	60°44'19.64"N	137°26'45.13"W	81 ± 6	380 ± 20	218 ± 12
HJ14	60°45'42.10"N	137°33'18.50"W	108 ± 12	469 ± 35	161 ± 12
HJ13	60°44'57.74"N	137°30'34.25"W	0.335154	0.31309, 0.358773	5.28
HJ14	60°46'31.55"N	137°34'45.88"W	0.629003	0.581476, 0.680414	9.36